Analytical Flutter Investigation of a Composite Propfan Model

K. R. V. Kaza* and O. Mehmed†
NASA Lewis Research Center, Cleveland, Ohio
G. V. Narayanan‡
Sverdrup Technology, Inc., Cleveland, Ohio
and
D. V. Murthy§
University of Toledo, Toledo, Ohio

This paper presents a theoretical model and an associated computer program for predicting flutter of propfans in subsonic axial flow. The model is based on two-dimensional unsteady cascade strip theory and three-dimensional steady and unsteady lifting surface aerodynamic theory in conjunction with a finite element structural model for the blade. The analytical results compare well with published experimental data. Parametric studies are also presented, illustrating the effects on flutter speed of blade-steady aeroelastic deformations, blade setting angle, rotational speed, the number of blades, structural damping, and the number of modes.

Nomenclature

$[A]$ = generalized aerodynamic matrix
a = elastic axis location
b = blade semichord
$\{F(t)\}$ = nonaerodynamic nodal force vector
$\{F_o\}$ = time-independent nonaerodynamic force vector
f_j = modal frequency of jth mode in Hz
$\{G\}$ = generalized motion-independent force vector
h = bending deflection
i = $\sqrt{-1}$
j = mode index, $j = 1, 2, 3, \ldots$
$[K_g]$ = generalized stiffness matrix, diagonal
$[K_s]$ = centrifugal softening matrix in physical coordinates
$[K(\{u\})]$ = nonlinear stiffness matrix in physical coordinates
M = Mach number
$[M]$ = physical mass matrix
$[M_g]$ = generalized mass matrix, diagonal
N = number of blades
$[P]$ = stiffness matrix defined in Eq. (10)
$\{P(\{u\},t)\}$ = aerodynamic nodal force vector
$\{P(\{u_o\})\}$ = steady-state aerodynamic nodal force vector
$\{q\}$ = vector of generalized coordinates
$\{q_o\}$ = amplitude of motion in generalized coordinates
$\{Q\}$ = generalized aerodynamic force vector
r = interblade phase angle index, $= 1, 2, \ldots, N$; also, distance from the axis of rotation
s = blade length along the reference line
t = time
$\{u\}$ = vector of blade deflections at grid points
$\{u_o\}$ = vector of steady-state deflections at grid points
$\{u_{o1}\}$ = steady-state deflectioans due to centrifugal loads
$\{u_{oi}\}$ = steady-state deflections after the ith iteration
V = free stream velocity
V_R = relative velocity
XYZ = global coordinate system
$X_1Y_1Z_1$ = blade fixed coordinate system
α = torsional deflection
$\beta_{0.75R}$ = blade pitch angle at the three-quarter radius
γ = eigenvalue defined in Eq. (10)
$\{\Delta F(t)\}$ = perturbation nonaerodynamic nodal force vector
$\{\Delta P^w(t)\}$ = perturbation aerodynamic nodal force vector (motion-independent)
$\{\Delta P(\{\Delta u\}, t)\}$ = perturbation aerodynamic nodal force vector (motion-dependent)
$\{\Delta u(t)\}$ = vector of vibratory deflections at grid points measured relative to $\{u_0\}$
ζ_j = structural damping ratio in jth mode
Λ = sweep angle
μ = real part of $i\sqrt{\gamma}$ (proportional to damping)
ν = imaginary part of $i\sqrt{\gamma}$ (flutter frequency)
σ_r = r-th interblade phase angle
$[\Phi]$ = modal matrix
ω = frequency
ω_j = frequency of jth mode
Ω = rotational speed

Subscripts

o = steady-state value
g = generalized (modal)
F = values at flutter point

Superscript

$\cdot$ = differentiation with respect to time
T = transpose

Presented as Paper 87-0738 at the AIAA/ASME/AHS/ASEE 28th Structures, Structural Dynamics and Materials Conference, Monterey, CA, April 6-8, 1987; received June 23, 1987; revision received Sept. 30, 1988.

*Senior Research Engineer. Associate Fellow AIAA.
†Research Engineer. Member AIAA.
‡Senior Engineer.
§NASA Resident Research Associate. Member AIAA.

Introduction

THE major goals of propfan designs are to maximize aerodynamic efficiency, minimize noise, and assure structural integrity. The aerodynamic and acoustic requirements of propfans have resulted in designs with thin, swept, and twisted blades of low aspect ratio and high solidity compared to conventional propellers. These blades operate in subsonic, transonic, and possibly supersonic flows. Furthermore, propfans may have a single rotor with blades rotating in one direction or two rotors rotating in opposite directions. The former is called a single-rotation (SR) propfan and the latter is called a counter-rotation (CR) propfan.

The unconventional features of the SR propfan add complexity to understanding the aeroelastic phenomena involved and in developing an analytical aeroelastic model. Since the blades are thin and flexible, deflections due to centrifugal and aerodynamic loads are large. Hence, the aeroelastic problem is inherently nonlinear, requiring geometric nonlinear theory of elasticity. Also, the blades are of low-aspect ratio with large sweep and, hence, require three-dimensional steady and unsteady aerodynamic models for accurate analysis. The blades have large sweep and twist, which couples blade bending and torsional motions, and are plate-like structures because of their low-aspect ratio. These factors require a finite element structural model that accounts for centrifugal softening and stiffening effects and possibly for Coriolis effects. The centrifugal softening terms are important because of large blade sweep and flexibility. The propfan rotor has four or more blades that necessitate the inclusion of aerodynamic coupling or cascade effects between the blades. The flexibility of the hub introduces additional structural coupling between the blades of a rotor. Furthermore, the aerodynamic and structural properties of the individual blades may differ from each other. The presence of these differences requires explicit consideration of both structural and aerodynamic mistuning in the analytical aeroelastic model. Additionally, for the CR propfan, there is aerodynamic interaction between the blades of the two rotors. Because of these unique features of both the SR and CR concepts, it is not possible to directly use the existing aeroelastic technology of conventional propellers, conventional turbofans, or helicopters.

As a part of the overall NASA single rotation propfan technology program, a series of 0.61-m (2-ft) diam, geometrically scaled models were tested in wind tunnels and on a NASA acoustic research aircraft. The tests and results are summarized in Ref. 1. Published literature on the CR concept is very limited; however, the benefits of the CR concept are discussed in Ref. 2. The present paper addresses the aeroelastic aspects of the SR propfan only.

Classical flutter of a SR propfan occurred unexpectedly during a previous wind tunnel performance experiment on a model (designated SR-5) with ten highly swept titanium blades. Reference 3 presented experimental flutter data of the SR-5 model and correlated the data with theory. In Ref. 3, the aerodynamic model is based on a two-dimensional unsteady cascade theory with a correction for blade sweep and the structural model is an idealized swept beam for each blade. References 4 and 5 refined the analytical model of Ref. 3 by using blade normal modes calculated from a finite-element plate model for the blade and correlated the refined analytical results with the flutter data of the SR-5 model. The correlation between theory and experiment in Refs. 3–5 varied from poor to good.

Additional subsonic wind tunnel flutter data, obtained by testing a composite propfan model, SR3C-X2 (Fig. 1), were presented in Ref. 6. A three-dimensional steady and unsteady aerodynamic theory for propfans with subsonic leading edge was presented in Ref. 7, and the theory was applied to predicting flutter for one test case of the wind tunnel model of Ref. 6.

The specific objectives of the present investigation are 1) develop a modal flutter analysis method that uses two- or three-dimensional steady and unsteady aerodynamics; 2) conduct parametric studies to ascertain the effect of steady airloads on frequencies, mode shapes, and flutter speed, and the effect of number of blades, blade setting angle, and blade structural damping on flutter speed; 3) validate the analytical models by correlating analytical and measured flutter speeds of the SR3C-X2 propfan model; and 4) examine the limitations of two-dimensional unsteady aerodynamic theory for propfan flutter analysis. To accomplish the objectives, a computer program ASTROP (Aeroelastic Stability and Response of Propulsion Systems) was developed. ASTROP was started with a two-dimensional unsteady aerodynamic theory corrected for blade sweep. This version is designated ASTROP2. Subsequently, it was enhanced by including three-dimensional steady and unsteady aerodynamics in a version called ASTROP3. ASTROP can be used with any finite element code that calculates blade steady-state deflections, mode shapes, and frequencies. Presently, COSMIC NASTRAN[8] is used. This paper describes the analytical method and the ASTROP code and presents parametric results that we believe will be useful for propfan designers and other investigators in the field.

The present work has been extended in Ref. 9 to include the effects of both structural and aerodynamic mistuning on propfan flutter.

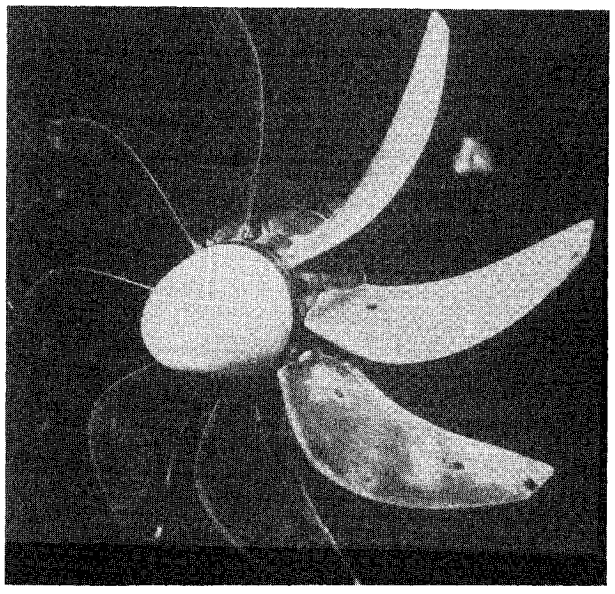

Fig. 1 SR3C-X2 propfan model in the Lewis 8 × 6 ft wind tunnel.

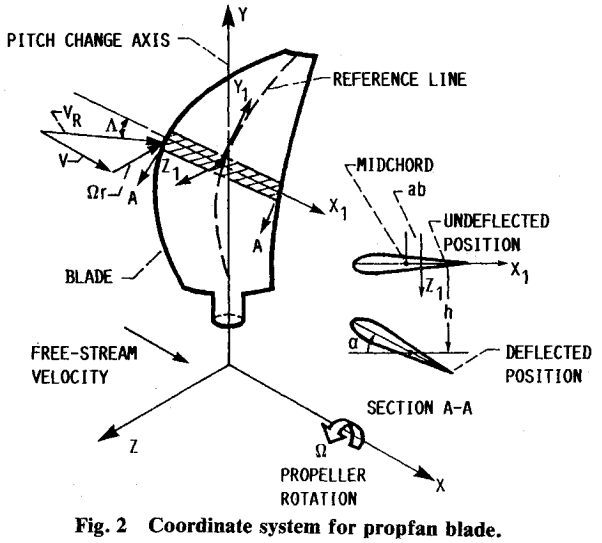

Fig. 2 Coordinate system for propfan blade.

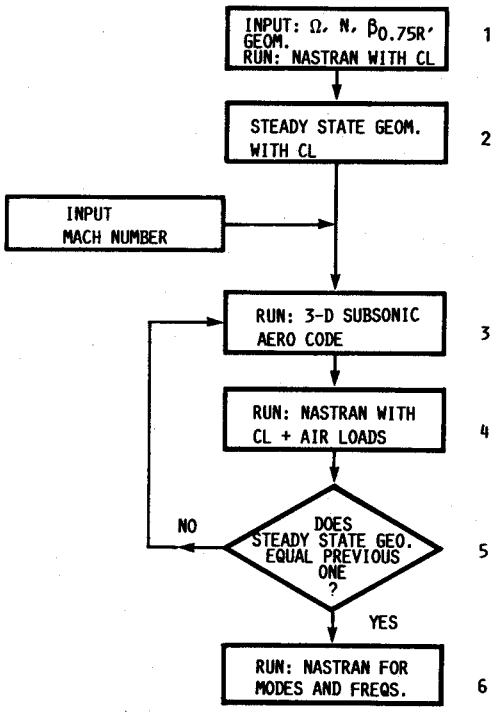

Fig. 3 Flow chart for calculating steady-state geometry, frequencies and mode shapes.

Analytical Formulation

The coordinate system used for developing the equation of motion of a rotating propfan blade is shown in Fig. 2. The propfan rotates about the X-axis, which is aligned with the frestream direction. The Y-axis is aligned along the blade pitch-axis and the Z-axis is perpendicular to the X-Y plane. Also shown in Fig. 2 are undeflected and deflected positions of an arbitrary blade strip that is normal to a reference line. The aeroelastic equation of motion of the blade can be written as

$$[M]\{\ddot{u}\} + [K_s]\{u\} + [K(\{u\})]\{u\} = \{P(\{u\},t)\} + \{F(t)\} \tag{1}$$

Because of the large deflections and the consequent need for the geometric nonlinear theory of elasticity in which the strain-displacement relations are nonlinear, the stiffness matrix $[K(\{u\})]$ is a function of nodal displacements and, hence, is nonlinear. The level of the geometric nonlinear theory of elasticity used herein, as well as in NASTRAN, is the one in which elongations and shears are negligible compared to unity. This explicit consideration of geometric nonlinear theory of elasticity provides the additional geometric differential stiffness due to centrifugal stiffening terms. The displacement dependent centrifugal softening terms are included in the matrix $[K_s]$, which is linear. The rotation also introduces Coriolis forces, but they are shown to be negligible for thin propfan blades in Ref. 10. Hence, they are not inlcuded in the present formulation.

Linearization of Equations

Equation (1) is generally nonlinear and is valid for calculating stalled and unstalled flutter speeds, forced response, aeroelastic performance, steady-state deflections, frequencies, and mode shapes. An appropriate solution method is to directly integrate in the time domain, but it is computationally inefficient. Common practice is to perturb it about a steady-state configuration by writing

$$\{u\} = \{u_o\} + \{\Delta u(t)\}$$

$$\{P(\{u\},t)\} = \{P(\{u_o\})\} + \{\Delta P(\{\Delta u\},t)\} + \{\Delta P^w(t)\}$$

$$\{F(t)\} = \{F_o\} + \{\Delta F(t)\} \tag{2}$$

where $\{u_o\}$, $\{P(\{u_o\})\}$, and $\{F_o\}$ are the steady-state values of $\{u\}$, $\{P(\{u\},t)\}$, and $\{F(t)\}$, respectively. The quantities $\{\Delta u(t)\}$, $\{\Delta P(\{\Delta u\},t)\}$, and $\{\Delta F(t)\}$ are perturbations from $\{u_o\}$, $\{P(\{u_o\})\}$, and $\{F_o\}$, respectively. The perturbation aerodynamic force is split into motion dependent ($\{\Delta P(\{\Delta u\},t)\}$) and motion independent ($\{\Delta P^w(t)\}$) parts for convenience in forced response analysis. Substituting Eq. (2) into the nonlinear Eq. (1) leads to two sets of equations: one steady-state equation for $\{u_o\}$ and another for the perturbation variable $\{\Delta u(t)\}$. These are

$$\left[[K_s] + [K(\{u_o\})]\right]\{u_o\} = \left\{P(\{u_o\})\right\} + \{F_o\} \tag{3}$$

$$[M]\{\Delta\ddot{u}(t)\} + \left[[K_s] + [K(u_o)]\right]\{\Delta u(t)\} = \left\{\Delta P(\{\Delta u\},t\right\} + \{\Delta P^w(t)\} + \{\Delta F(t)\} \tag{4}$$

Steady-State Configuration and Vibration Analysis

The steady-state configuration for a given rotational speed and Mach number is obtained by solving the nonlinear Eq. (3) (see Fig. 3). The stiffness matrix $[K(\{u_o\})]$ includes elastic stiffness and differential stiffness, due to centrifugal stiffening loads and steady-state aerodynamic loads. Once the steady-state deflection and the effective total stiffness are known from Eq. (3), the vibration frequencies and mode shapes are calculated by solving

$$[M]\{\Delta\ddot{u}(t)\} + [[K_s] + [K(\{u_o\})]]\{\Delta u(t)\} = 0 \tag{5}$$

which leads to the generalized mass matrix $[M_g]$, the modal matrix $[\Phi]$, and the modal frequencies ω_j.

Flutter and Forced Response by the Modal Method

The general vibratory motion can be expressed as a superposition of the contributions of the various normal modes:

$$\{\Delta u(t)\} = [\Phi]\{q\} \tag{6}$$

Substituting Eq. (6) into Eq. (4) and postmultiplying the result by $[\Phi]^T$ leads to

$$[M_g]\{\ddot{q}\} + [K_g]\{q\} = [A]\{q\} + \{G(t)\} \tag{7}$$

where

$$[M_g] = [\Phi]^T[M][\Phi]$$

$$K_{gjj} = M_{gjj}\omega_j^2(1 + 2i\zeta_j)$$

$$[A]\{q\} = [\Phi]^T\{\Delta P(\Delta u,t)\}$$

$$\{G(t)\} = [\Phi]^T[\{\Delta F(t)\} + \{\Delta P^w(t)\}] \tag{8}$$

The order of Eq. (7) depends on the number of modes included in Eq. (6). This number is determined by performing numerical experiments, which will be explained later. The structural damping in each mode is introduced through the damping ratio ζ_j, where the modal index $j = 1,2,3,\ldots$ The generalized aerodynamic matrix is represented by $[A]$ for each interblade phase angle for simple harmonic motion of the blade. The motion independent aerodynamic and nonaerodynamic forces are represented by $\{G(t)\}$ for each interblade phase angle. This is included for completeness in the formulation, but no results on forced response will be presented in this paper. For simple harmonic motion the flutter eigenvalue problem can be rewritten from Eq. (7) after setting $\{G(t)\} = \{0\}$ as

$$[P]\{q_o\} = \gamma[M_g]\{q_o\} \tag{9}$$

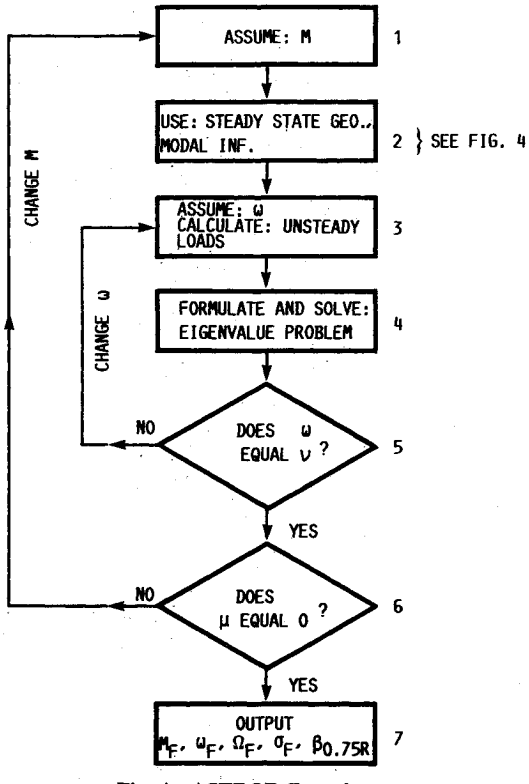

Fig. 4 ASTROP flow chart.

where

$$\{q\} = \{q_o\}e^{i\omega t}$$

$$[P] = [K_g] - [A]$$

$$i\sqrt{\gamma} = i\omega = \mu + i\nu \tag{10}$$

Flutter occurs when $\mu > 0$.

ASTROP Computer Code

The ASTROP code is based on the normal mode method and is for classical flutter, forced response, and whirl flutter analysis of propulsion systems. Only the classical flutter part of the code that uses two-dimensional subsonic unsteady aerodynamics (ASTROP2) and three-dimensional subsonic steady and unsteady aerodynamics (ASTROP3) is used in the present investigation.

ASTROP2

The input to ASTROP2 and the steps involved for solving the flutter problem are shown in the flow chart in Fig. 4. The input consists of blade geometry described by the grid point coordinates in the XYZ system (Fig. 2) and the modal information—frequencies, mode shapes, and generalized masses. For calculating modal information, the equivalent anisotropic material properties for each element are generated by using a preprocessor code COBSTRAN.[11] The main step, which is no. 3 in Fig. 4, is the calculation of the generalized aerodynamic matrix $[A]$ by using normal modes and an aerodynamic strip representation of the blade. The blade is divided into a series of discrete aerodynamic strips, each of constant properties. One of these strips is shown in Fig. 2. Each swept strip has two motions, plunging and pitching about an arbitrary reference line, that are expressed in terms of normal modes and normal coordinates. The gap-to-chord ratio, sweep angle, and blade pitch angle are calculated from the steady-state configuration. The lift and moment equations for each section are obtained by extending the unsteady equations for a swept wing (generated in Ref. 12) to a linear cascade case. This extension was implemented for the first time in Ref. 3. There was no correction for the tip effects. Further details about the aerodynamic model and numerical procedures are given in Ref. 15.

Next, the flutter problem described in Eq. (10) is solved in step 4 of Fig. 4; steps 2–4 are repeated until the conditions in steps 5 and 6 are met. Finally, the critical flutter variables are extracted in step 7. The main limitations of the analytical model used in the code are: 1) the validity of aerodynamic strip theory for propfans; 2) the validity of the sweep correction in the presence of cascade effects; 3) the arbitrariness of the reference line; and 4) the approximation involved in calculating h and α and their derivatives along the reference line from the normal modes.

ASTROP3

This version of the code consists of three branches. The blade steady-state pressures, generalized unsteady aerodynamic forces and stability, and forced response due to yawed-flow are calculated in branches one, two, and three, respectively. Only the first two branches are shown in the form of a flow chart in Figs. 3 and 4, respectively, because forced response is not addressed in the present paper. This is an expanded and modified version of the code described in Ref. 7. The structural model is again based on a finite element approximation. The aerodynamic analysis is based on three-dimensional linearized compressible lifting surface theory in which mean loading effects, blade stall, and transonic shock waves are not included. The analysis ignores blade thickness and evaluates the load distribution on the rotor for simple harmonic motion of the blade camber surfaces using a piece-wise constant pressure panel method. Input to the aerodynamic analysis consists of the mean camber surface geometry and the normal mode displacement vectors generated by the finite element structural model. A version of the code accounting for supersonic tip Mach numbers is under development. All of the cases analyzed here are at subsonic relative Mach numbers.

The input to ASTROP3 and the solution procedure are almost the same as those for ASTROP2. However, the effect of steady three-dimensional airloads is included in calculating the steady-state configuration and the differential stiffness in steps 3–5 of Fig. 3. This feature also provides the steady aeroelastic performance at each iteration of the nonlinear solution of Eq. (3). The performance results can be printed in step 5 of Fig. 3.

The iterative-interaction process, steps 3–5, is continued until the deflection from the $(i+1)^{th}$ iteration converges to that from the i^{th} iteration. Then, the frequencies and mode shapes are calculated in step 6.

The generalized aerodynamic coefficient matrix $[A]$ is calculated in step 3 of Fig. 4 by using the procedure outlined in Ref. 7. The eigenvalue problem in step 4 is repeated until the flutter conditions in steps 5 and 6 are met. The entire procedure is repeated for each interblade phase angle and the critical flutter variables are printed in step 7.

Results and Discussion

A propfan flutter research model, Fig. 1, SR3C-X2, is analyzed using ASTROP3. The blades are made from graphite-ply/epoxy-matrix material. There are eight blades on the rotor. The geometric midchord sweep is 45 deg at the tip and the tip diameter is 0.61 m (2 ft). The blade mass ratio is approximately 33. The model has been tested for flutter at various rotational speeds, freestream Mach numbers, and blade setting angles. The model was designed for a Mach number of 0.8, but it was not reached during the tests because of flutter. Measured advance ratios and power coefficients at flutter for the conditions to be discussed are between 2.0 and 4.0, and 0.0 and 2.6, respectively. Details on the model and flutter data can be found in Ref. 6.

The finite element model of the blade used in the analyses consists of 228 grid points and 388 plate elements. The hub that retains the blades is assumed rigid and is not modeled.

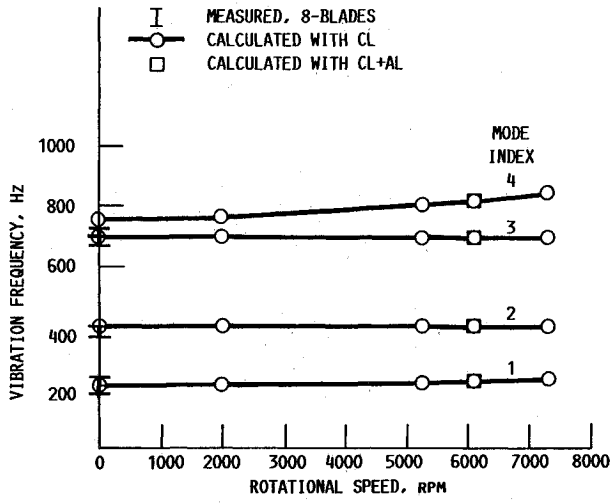

Fig. 5 Variation of blade natural frequencies with rotational speed $\beta_{0.75R}$ = 61.6 deg, cosmic NASTRAN.

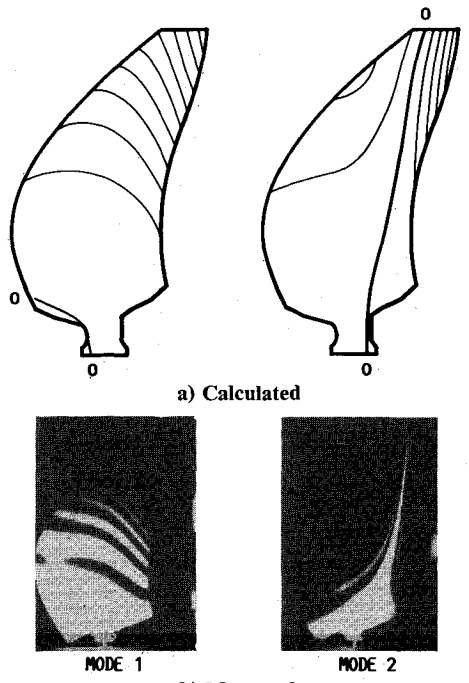

Fig. 6 Comparison of calculated and measured mode shapes.

Also, all the blades are assumed to be aerodynamically, geometrically, and structurally identical. Consequently, it is adequate to model one blade and to analyze each interblade phase angle independently. The effects of nonidentical blade properties are addressed in Ref. 9.

Frequencies and Mode Shapes

Figure 5 shows the variation of the SR3C-X2 blade natural frequencies with rotational speed in vacuum. The measured bench natural frequency band of the eight blades is shown for comparison. The frequencies are calculated with centrifugal loads (CL) for all rotational speeds and with centrifugal loads and steady three-dimensional airloads (CL + AL) at 6100 rpm by the procedure described in Fig. 3. Figure 6 shows measured and calculated constant displacement contours of the blade modes. Only the first two modes are included because it will be shown later that the flutter mode is a combination of the first two modes. The nodes are marked 0-0 on the calculated contours. It can be seen from Fig. 5 that the measured and calculated frequencies for the first mode correlate but the measured frequencies for the second, third, and fourth modes are lower

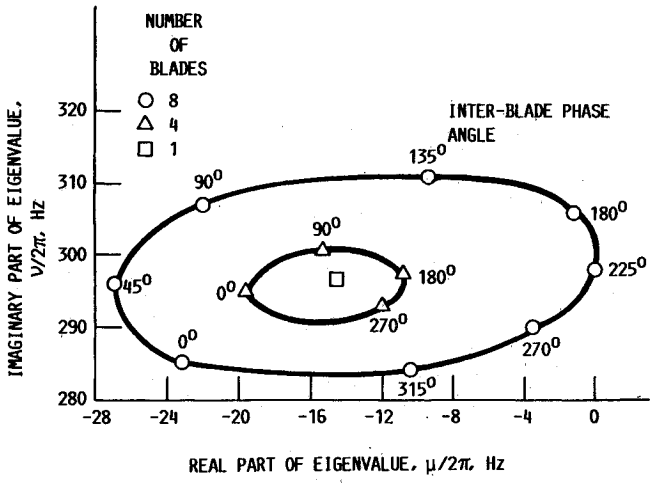

Fig. 7 Root locus plot of the mode with least damping: M = 0.59, Ω = 6080 rpm, $\beta_{0.75R}$ = 61.6 deg.

than the calculated ones. Also, the steady airloads do not have a significant effect on the frequencies. The first mode frequency increases with an increase in rotational speed. This trend is expected because of centrifugal stiffening. The second and third mode frequencies do not change significantly with rotational speed. It can be seen from the contour plots (Fig. 6) that the first mode is primarily flatwise bending but also has a large degree of torsion, and that the second mode is primarily torsion near the tip. The correlation between theory and experiment for the first two modes is reasonably good and for the higher modes the correlation is poor. The difference between the average measured (375 Hz) and the calculated frequency (399 Hz) for the second mode is attributed to unknowns in blade properties due to manufacture and/or root effects. Even though the effect of steady aerodynamic loads on frequencies is small, its effect on deflection, particularly at the tip, is appreciable in some cases and will be discussed later.

Effect of Unsteady Cascade Aerodynamics on Blade Flutter

To illustrate the effect of cascade aerodynamics on flutter, the real and imaginary parts of the eigenvalues of the critical flutter mode of the SR3C-X2 wind tunnel model are shown in Fig. 7. These results are obtained by using the procedure described in Fig. 4 without steady airloads. The eigenvalues for all the interblade phase angles are shown at the critical freestream Mach number and frequency. Since there are eight blades there are eight interblade phase angles, $\sigma_r = 360r/8$, where the phase index $r = 0,1, \ldots 7$. Figure 7 may be interpreted as a root locus of the interblade phase angle modes. For comparison, the root loci for a four-blade and a single-blade case are also included in Fig. 7. Because of the aerodynamic interaction (cascade effect) between the blades, the one eigenvalue of the single-blade case splits into four and eight for the four and eight blade cases, respectively. When these points are joined, a rough ellipse is formed for each case. The destabilizing influence of the cascade effect is indicated by the length of the semimajor axis of the ellipse. The results clearly show that the cascade effect is very significant even for the case of four blades. This is confirmed by the experiment, as will be shown later. The other point to be noted from this figure is that the most critical flutter interblade phase angle for the eight blade case is 225 deg, which is a three nodal diameter backward traveling wave in the notation employed herein, and that for the four blade case it is 180 deg.

Effect of Freestream Mach Number on Effective Modal Damping

Figure 8 shows the variation of the real part of the eigenvalue with freestream Mach number at Ω = 6080 rpm, $\beta_{0.75R}$ = 61.6 deg, and σ_r = 225 deg. The real part of the eigenvalue is plotted for the critical flutter mode only. The negative

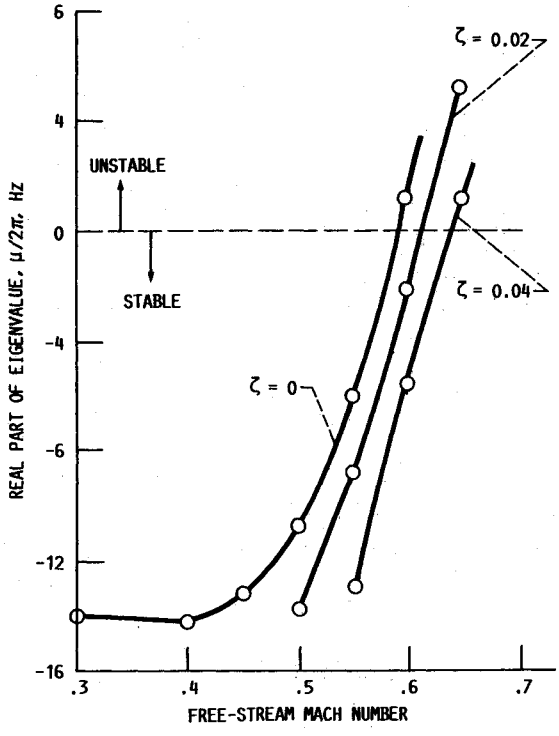

Fig. 8 Variation of damping with Mach number: $\Omega = 6080$ rpm, $\beta_{0.75R} = 61.6$ deg, $\sigma_r = 225$ deg, $N = 8$.

of the real part of the eigenvalue is proportional to modal damping. For the case of no structural damping, $\zeta = 0$, the real part of the eigenvalue is almost constant for Mach numbers between 0.3 and 0.4 and starts increasing rapidly for M between 0.4 and 0.6.

Effect of Structural Damping

As mentioned earlier, structural damping is introduced into the analysis [Eq. (8)] through the viscous damping ratio. The effect of structural damping on the real part of the eigenvalues is also included in Fig. 8. It can be seen from the figure that a structural damping ratio ζ of 0.02 in each mode has increased the flutter Mach number from 0.595 to 0.615. Also, the results show that a structural damping ratio of 0.04 in each mode increases the effective damping ratio (the ratio of the real and imaginary parts of the eigenvalue) only to about 0.02 for the critical mode. Thus, the effective damping is not increased by the full amount of the added structural damping. The value of the structural damping ratio for composite blades of the SR3C-X2 model is of the order of 0.02. Since the value of ζ and the consequent increase in flutter Mach number for the SR3C-X2 blades are small, all the analytical predictions in this paper are made with $\zeta = 0$. Consequently, the analytical results are slightly conservative.

Comparison of Calculated and Measured Flutter Boundary

The calculated flutter boundaries are compared with measured boundaries in Figs. 9 and 10 for eight- and four-blade cases, respectively. The flutter boundary is shown as a variation of freestream flutter Mach number with rotational speed with blade pitch angle as a parameter. Figure 9 includes blade pitch angles 61.6, 56.6, and 68.4 deg, and Fig. 10 includes those at 61.6 and 56.6 deg. The steady-state blade configurations that are used in the study are: 1) the undeflected position UP; 2) deflected position with centrifugal loads CL; and 3) deflected position with centrifugal and three-dimensional steady airloads CL + AL. The possible perturbation cases are designated by modes and frequencies, and these are: 1) with centrifugal loads, CL, 2) with centrifugal loads and measured second mode frequency, CL and $f_2 = 375$ Hz, 3) with centrifugal loads and three-dimensional airloads, CL + AL, and 4) same as three with $f_2 = 375$ Hz. The case with $f_2 = 375$ Hz is included because the measured nonrotating frequency for the second mode is 375 Hz and the calculated value is 399 Hz. Since the second mode frequency, as shown by theory in Fig. 5, is independent of rotational speed, the nonrotating measured value is used in the flutter speed calculations. To minimize computational time, all these configurations and perturbation cases are considered only for $\beta_{0.75R} = 61.6$ deg, which is the steady-state blade angle at the design point.

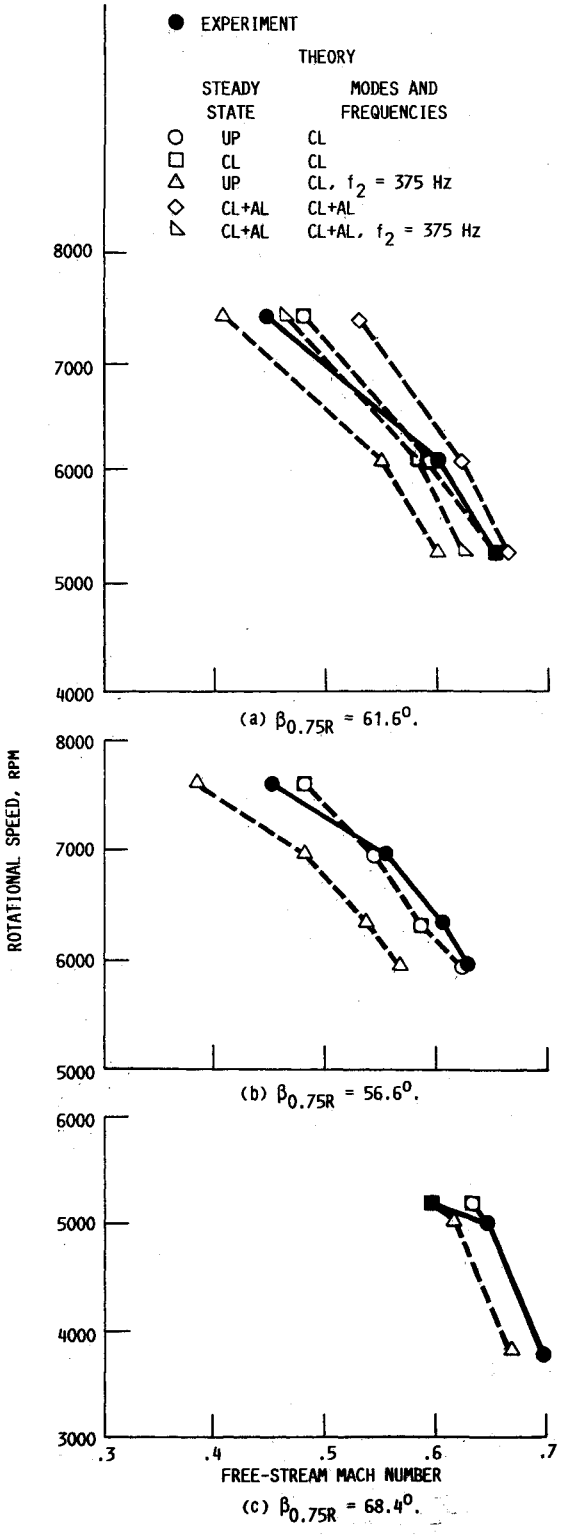

Fig. 9 Comparison of measured and calculated flutter boundary, eight blades.

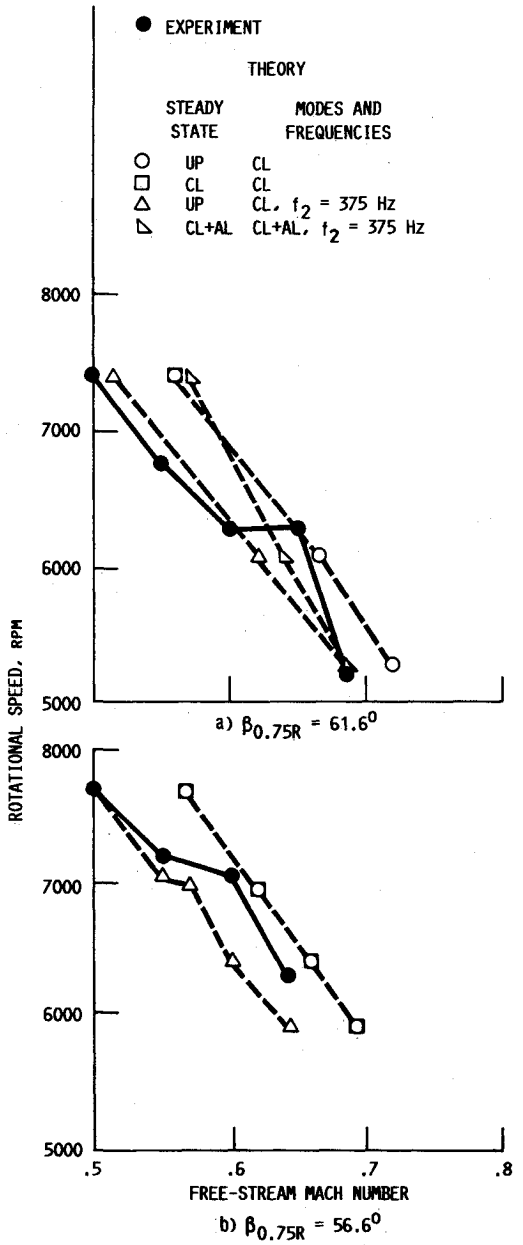

Fig. 10 Comparison of measured and calculated flutter boundary, four blades.

Correlation of Calculated and Measured Flutter Mach Numbers

Comparing the measured Mach numbers with the calculated ones in Fig. 9a for $\beta_{0.75R} = 61.6$ deg, with UP as the steady state and the CL as the perturbation state, the correlation between theory and experiment is very good for $\Omega = 5280$ and 6080 rpm. However, the calculated Mach number for $\Omega = 7320$ rpm is slightly higher than the measured value. A similar comparison with the same steady and perturbation states in Fig. 9b for $\beta_{0.75R} = 56.6$ deg and in Fig. 9c for $\beta_{0.75R} = 68.4$ deg also shows very good agreement between theory and experiment. The predicted slope of the flutter boundary line for all the blade pitch angles agrees well with that of the experiment. Both theory and experiment show that for a given rpm the freestream flutter Mach number decreases with an increase in the blade pitch angle. For example, when $\Omega = 6000$ rpm, the experimental flutter Mach number is 0.62 for a blade pitch angle of 56.6 deg (Fig. 9b), and 0.6 for a pitch angle of 61.6 deg (Fig. 9a).

The comparisons made in Fig. 9 for eight blades with the steady state UP and the perturbation state CL are repeated in Fig. 10 for four blades and a pitch angle of 61.6 deg. As can be seen, the correlation between theory and experiment again is very good. However, the difference between the calculated and measured flutter Mach numbers for the four-blade case is slightly greater. It implies that the theory may be overcorrecting for the aerodynamic cascade effects for the four-blade case.

Sensitivity of Fluter Mach Number to Frequency

Comparison of calculated flutter Mach numbers with the steady-state UP and the perturbation state as CL with corresponding calculated ones with the same steady state and the perturbation state and $f_2 = 375$ Hz shows that the flutter speed is very sensitive to change in the second-mode frequency for all the cases in Figs. 9 and 10. For example, the flutter Mach number decreased from 0.6 to 0.55 at $\Omega = 6080$ rpm (Fig. 9a) when the second mode frequency is reduced from 399 to 375 Hz. Comparing the calculated flutter Mach numbers with the steady-state UP and the perturbation state CL, $f_2 = 375$ Hz with the corresponding measured ones in Figs. 9 and 10, we find that the calculated Mach numbers are slightly less than the measured ones except when the blade pitch angle is 61.6 deg with four blades (Fig. 10a). In this case, the experimental boundary is closer to the calculated one. Also, as can be seen in Figs. 10a and 10b, there is a kink in the measured flutter boundary, and the kink was predicted in Fig. 10b by taking a smaller step in rotational speed. The precise reason for the kink is not known.

Effect of Centrifugal Loads and Steady Airloads on Flutter

The analysis procedure described in Fig. 3 is used to calculate the blade steady-state position with centrifugal loads and steady airloads (hot shape). This is a geometric nonlinear analysis. It was found that the centrifugal loads twist the blades toward flat pitch and this twist increases with rotational speed. For example, the change in blade angle ($0.75R$) from the undeflected to the deflected position for 6080 rpm is 1.7 deg, and for 7400 rpm it is 2 deg. The aerodynamic loads cause an additional twist of approximately 0.65 deg for 7400 rpm and $M = 0.5$. This twist may have a significant effect on flutter. To study the effect of blade steady-state position, first only centrifugal loads, and then both centrifugal and aerodynamic loads were applied to the blades. The aerodynamic loads were updated in the deflection analysis until a converged steady-state deflected position was obtained. The converged position is designated by CL + AL. First, the effect of centrifugal loads will be discussed. Calculated flutter Mach numbers with the steady-state UP and the perturbation CL are compared in Figs. 9 and 10 with the corresponding calculated ones with the steady and perturbation states as CL for all the blade pitch angles. The results show that the change in the steady state from UP to the CL does not have an appreciable effect on flutter Mach numbers. Now, the effect of both centrifugal and aerodynamic loads will be discussed. Flutter Mach numbers calculated with the CL for both the steady and perturbation states are compared in Fig. 9a with the corresponding ones with the CL + AL for both the steady and perturbation states. It is evident from the results that the steady airloads have a significant influence on flutter speed. The influence increases with increasing rotational speed. For example, the increase in predicted Mach number is 0.01 at $\Omega = 5280$ rpm, 0.02 at $\Omega = 6080$ rpm, and 0.05 at $\Omega = 7370$ rpm. Even though the change in the modal frequencies due to steady-state airloads is small, there is a significant change in blade camber and mode shapes at higher rpm. Thus, the increase in flutter speed at higher rpm due to steady airloads is attributed to 1) small changes in modal frequencies, 2) mode shape changes, and 3) change in blade steady-state angle, and, hence, blade pitch angle. The change in flutter Mach number due to a reduction in the second-mode blade frequency from 399 to 375 Hz is about the same with and without steady airloads in Fig. 9a. The theoretical boundary in Fig. 9a that is closest to the experimental is the one for which CL + AL is the steady state and

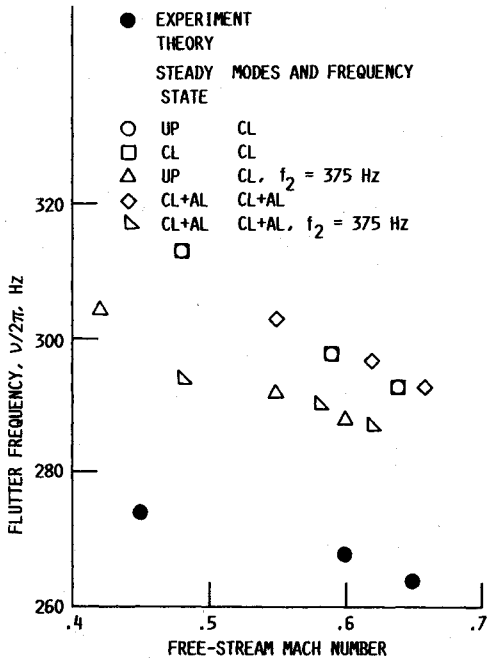

Fig. 11 Comparison of measured and calculated flutter frequencies, eight blades, $\beta_{0.75R}$ = 61.6 deg.

CL + AL and f_2 = 375 Hz is the perturbation state. Comparing these boundaries, the correlation is very good.

Effect of Number of Modes on Flutter Analysis

The effect of varying the number of modes from two to six in the perturbation analysis presented in Figs. 9 and 10 was investigated. It was found that there is no appreciable effect on flutter speed by increasing the number of modes beyond two. In other words, the flutter mode is a combination of first and second natural modes and there is very little participation of higher modes.

Correlation of Measured and Calculated Flutter Frequencies

Measured and calculated flutter frequencies for the configurations described in Fig. 9a are compared in Fig. 11. In general the calculated flutter frequency is higher than the measured value. The correlation between theory and experiment is better when the second-mode frequency is corrected to 375 Hz and when steady-state aerodynamics are included. Even for this case, the calculated flutter frequencies are approximately 7% higher than measured. A similar correlation was noticed for other blade setting angles and for four-bladed cases, but they are not shown.

Correlation of Measured and Calculated Flutter Interblade Phase Angles

Another important parameter for propfan flutter is the interblade phase angle. The calculated flutter interblade phase angle for eight blades and $\beta_{0.75R}$ = 61.6 deg is 225 deg which corresponds to a three-nodal diameter backward traveling wave. The predominant measured value is also 225 deg. However, the measured value is slightly off from 225 deg for some blades. This is possibly caused by the inherent mistuning that was present in the rotor. The same type of correlation between theory and experiment was noticed at other rotational speeds and, hence, those results are not shown. For a blade setting of 56.6 deg, two interblade phase angles, 180 and 225 deg are present in the measured flutter mode. The frequencies of the two interblade angle modes are slightly different. Surprisingly, theory also predicted the presence of the two interblade phase

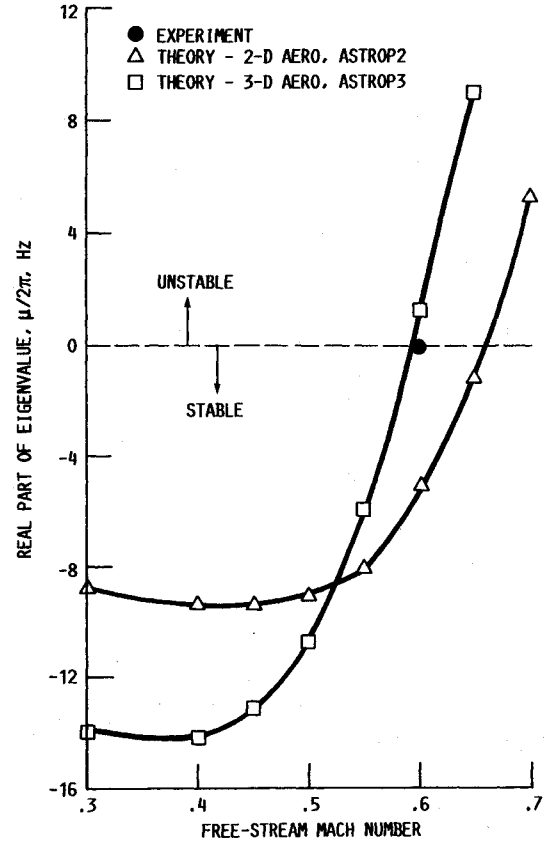

Fig. 12 Comparison of two- and three-dimensional unsteady aerodynamic theories: Ω = 6080 rpm, $\beta_{0.75R}$ = 61.6 deg.

angles and the correlation is extremely good. Furthermore, it is apparent from the results that the flutter interblade phase angle is a function of blade setting angle.

For the four-bladed rotor, the correlation between the measured and calculated interblade phase angles is also very good. Here, the predominant interblade phase angle both in experiment and theory is 180 deg for all blade setting angles and rotational speeds considered in Fig. 10.

Evaluation of Two-Dimensional Unsteady Aero For Flutter Prediction

To assess the validity of two-dimensional aerodynamic theory and the associated sweep correction, the real parts of the eigenvalue of the critical mode calculated by using both two- and three-dimensional theories are compared in Fig. 12; also included in this figure is the measured flutter Mach number. In the ASTROP2 code, which uses two-dimensional aerodynamics, the reference line of the blade (Fig. 2a) is somewhat arbitrary. Also, the sweep of each strip depends on the reference line. In the present calculations, the leading edge is used as reference line. From the results, it is evident that the two-dimensional theory is less accurate than the three-dimensional theory in predicting the flutter Mach number. Correlative studies were also conducted by varying freestream Mach number, blade sweep, rotational speed, and blade setting angle. The correlation varied from poor to good. In some cases the expected conservative nature of the two-dimensional theory did not prevail, possibly because of the arbitrariness of the reference line and the associated aerodynamic sweep correction. The computational time for evaluating the unsteady aerodynamic loads using two-dimensional theory (with six stations along the span) was found to be about 65% of the time using the three-dimensional theory. Hence, it is concluded that the three-dimensional theory should be preferred to the two-

dimensional theory, since more accuracy can be obtained without a significant increase in computational cost.

Conclusions

A theoretical model and an associated computer program were developed for predicting subsonic flutter of propfans. Theoretical results were correlated with published measured data. These correlations and additional parametric results led to the following conclusions:

1) In general, the agreement between theory and experiment in predicting flutter speeds and interblade phase angles is very good. However, the predicted flutter frequencies with three-dimensional unsteady aerodynamic theory are slightly higher than those measured.

2) The flutter speed predicted by three-dimensional unsteady aerodynamic theory is more accurate than that predicted by two-dimensional theory. Since the computational time of three-dimensional theory is not significantly greater than that of two-dimensional theory, three-dimensional theory should be preferred for flutter analysis.

3) The influence of steady-state aerodynamics on the blade steady-state configuration, mode shapes, and flutter is significant in some cases. Thus, it should be included in the final design calculations.

4) Both theory and experiment showed that increasing the number of blades on the rotor is destabilizing. This is believed to be caused by a change in aerodynamic coupling between blades. Thus, aerodynamic cascade effects should be included in the analysis.

5) Both theory and experiment showed that increasing the blade setting angle is destabilizing. This is inferred due to a change in the aerodynamic coupling between blades (because of the change in the relative orientation of the blades) and a change in blade frequencies and modes shapes (because of the change in steady-state blade loading).

6) For the rotor considered, the flutter mode is dominated by the first two-blade normal modes and there is strong coupling between the two modes.

7) Both theory and experiment showed that under certain conditions two interblade phase angle modes with slightly different frequencies may be present during flutter. Furthermore, the flutter interblade phase angle is a function of blade setting angle and number of blades on the rotor.

References

[1]Mikkelson, D. C., Mitchell, G. A., and Bober, L. J., "Summary of Recent NASA Propeller Research," NASA TM-83733, Oct. 1984.

[2]Strack, W. C. et al., "Technology and Benefits of Aircraft Counter Rotation Propellers," NASA TM-82983, Oct. 1982.

[3]Mehmed, O., Kaza, K. R. V., Kielb, R. E., and Lubomski, J. F., "Bending-Torsion Flutter of a Highly Swept Advanced Turboprop," NASA TM-82975, Oct. 1982.

[4]Elchuri, V. and Smith, G. C. C., "Flutter Analysis of Advanced Turbopropellers," *AIAA Journal,* Vol. 22, June 1984, pp. 801–802.

[5]Turnburg, J. E., "Classical Flutter Stability of Swept Propellers," AIAA Paper 83-0847, May 1983.

[6]Mehmed, O. and Kaza, K. R. V., "Experimental Classical Flutter Results of a Composite Advanced Turboprop Model," NASA TM-88972, July 1986.

[7]Williams, M. H. and Hwang, C., "Three-Dimensional Unsteady Aerodynamics and Aeroelastic Response of Advanced Turboprops," *AIAA 27th Structures, Structural Dynamics, and Materials Conference,* Part 2, AIAA, New York, 1986, pp. 116–124.

[8]The NASTRAN Theoretical Manual, NASA SP-221(06), 1981.

[9]Kaza, K. R. V., Williams, M. H., Mehmed, O., and Moss, L. E., "Analytical and Experimental Investigation of Mistuning on Advanced Propfan Flutter," AIAA Paper 87-0739, April 1987.

[10]Subrahmanyam, K. B., Kaza, K. R. V., Brown, G. V., and Lawrence, C., "Nonlinear Bending-Torsional Vibration and Stability of Rotating, Pretwisted, Preconed Blades Including Coriolis Effects," NASA TM-87207, Jan. 1986.

[11]Chamis, C. C., "Integrated Analysis of Engine Structures," NASA TM-82713, Nov. 1981.

[12]Barmby, J. G., Cunningham, H. J., and Garrick, I. E., "Study of Effects of Sweep on the Flutter of Cantilever Wings," NACA TN-2121, June 1950.

[13]Kaza, K. R. V. and Kielb, R. E., "Flutter and Response of a Mistuned Cascade in Incompressible Flow," *AIAA Journal,* Vol. 20, Aug. 1982, pp. 1120–1127.

[14]Rao, B. M. and Jones, W. P., "Unsteady Airloads for a Cascade of Staggered Blades in Subsonic Flow," *Unsteady Phenomena in Turbomachinery,* AGARD CP-177, AGARD, France, 1976, pp. 32-1 to 32-10.

[15]Kaza, K. R. V., Mehmed, O., Narayanan, G. V., and Murthy, D. V., "Analytical Flutter Investigation of a Composite Propfan Model," NASA TM-88944, April 1987.